Interface control of a morphotropic phase boundary in epitaxial samarium modified bismuth ferrite superlattices

Ronald Maran,[1,*] Shintaro Yasui,[2] Eugene A. Eliseev,[3] Maya D. Glinchuk,[3] Anna N. Morozovska,[3] Hiroshi Funakubo,[2] Ichiro Takeuchi,[4,†] and Valanoor Nagarajan[1,‡]

[1]*School of Materials Science and Engineering, The University of New South Wales, Sydney 2052, Australia*

[2]*Department of Innovative and Engineered Materials, Tokyo Institute of Technology, 4259 Nagatsuta-cho, Midori-ku, Yokohama 226-8502, Japan*

[3]*Institute for Problems of Materials Science, NAS of Ukraine, Krjijanovskogo 3, 03142 Kiev, Ukraine*

[4]*A. James Clark School of Engineering, University of Maryland, College Park, Maryland 20742, USA*

Interfacial control of a polar-(rhombohedral) to-non-polar (orthorhombic) phase transition in (001)-oriented epitaxial $BiFeO_3/(Bi_{1-x}Sm_x)FeO_3$ superlattices is presented. We demonstrate controlling the composition at which a polar phase transformation takes place by tuning the strength of the interlayer interactions while holding the average composition constant. It is shown that the thickness of the superlattice layers has a strong influence on the interlayer polar coupling, which in turn changes the phase transition. For the shortest periods studied (layers 5- and 10-nm thick) the onset of the phase transition is suppressed along with a significant broadening (as a function of Sm^{3+} concentration) of an incommensurately modulated phase determined by two-dimensional x-ray diffraction mapping. Consequently, a ferroelectric character with robust polarization hysteresis and enhanced dielectric constant is observed even for substitution concentration of Sm^{3+} which would otherwise lead to a leaky paraelectric in single-layer $(Bi_{1-x}Sm_x)FeO_3$ films. The experimental results are fully consistent with a mean-field thermodynamic theory which reveals that the strength of the interlayer coupling is strongly affected by the polar-polar interaction across the interface.

PACS number(s): 77.80.bn, 77.55.Nv, 77.55.Px

I. INTRODUCTION

Interface engineering has emerged as a rich and fertile approach to tune functional properties in epitaxial perovskite thin films [1]. Interface control of properties in perovskites is best exemplified in epitaxial superlattices where alternating layers of two or more different perovskite compounds are stacked along the growing axis [2]. The underpinning rationale here is that the imposed geometric constraint forces the neighboring layers to physically interact with each other and thus yield phases and properties that may simply not exist in the constituent parents. In the special case of polar dielectrics and ferroelectrics (FEs), some of the prominent examples include the emergence of ferroelectricity [3,4], giant dielectric permittivity [5] and electromechanical coefficients [6], enhanced multiferroic behavior [7], and strong second-harmonic signal generation [8]. It is well known that electrical [9,10] and mechanical boundary conditions [11,12] significantly influence the ultimate polar phase stabilization and subsequent ferroic property enhancement. The occurrence of such phenomena has been confirmed by both the mean-field Landau-Ginzburg-Devonshire theory [13] and the first-principles approaches [14]. Furthermore, for short period superlattices not only the imposed mechanical strain is translated from one layer to the other without relaxation (i.e., pseudomorphic conditions of constraint), but also the polarization may be continuous [15]. In such a case the electrostatic coupling significantly governs the overall ferroic phase behavior.

One aspect that has garnered attention is the inducement of a ferroic phase transition using the superlattice engineering approach. It opens new ways to artificially create phase boundaries where often the dielectric susceptibilities as well as the electromechanical coefficients are enhanced [3–15]. For example, Dawber and co-workers [15–17] have reported on the tailoring of ferroelectric/paraelectric superlattices to control the ferroelectric-paraelectric phase transition and hence the polarization behavior depending on the superlattice component thicknesses [3]. This approach was further extended to where polar competition in combination with strain engineering was exploited to achieve polarization rotation in artificially layered epitaxial superlattices [17]. In doing so, a morphotropic phase boundary- (MPB-) like material was created for a superlattice whose average composition would, by itself, nominally be a single tetragonal phase in the solid-solution phase diagram. This is immensely useful as a maximum in the dielectric permittivity, and the piezoelectric coefficient d_{33} was realized. They thus established that with a careful choice of materials and tuning of superlattice fractions, it is indeed possible to induce a phase transition that may not be exhibited in the bulk compound.

Recently using a combinatorial pulsed laser deposition (PLD) approach, we observed a universal phase transition behavior for rare-earth- (RE-) doped $BiFeO_3$ (BFO) thin films [18,19]. Investigations into the substitution of various trivalent RE dopants into the A site of $BiFeO_3$ established that irrespective of the RE dopant used, a structural transition from the ferroelectric rhombohedral-(R) phase to a nonpolar orthorhombic-(O) phase (hereafter referred to simply as $R \to O$ phase transition) takes place. This was identified to be a FE-antiferroelectric (AFE-) MPB based on an earlier

*r.maran@student.unsw.edu.au

†takeuchi@umd.edu

‡nagarajan@unsw.edu.au

245131-1

framework given by Baloshova and Tagantsev [20] and Diéguez *et al.* [14]. The application of the electric field induces an electric-field-driven transformation from the nonpolar O phase to the polar R phase at this structural phase boundary, which gives rise to a double hysteresis in the polarization-electric-field (hereinafter referred to as *P-E*) loop. As a consequence of this electric-field-induced phase transition at this phase boundary, a substantial enhancement of electromechanical properties was observed. This includes an increase in the effective piezoelectric coefficient d_{33} to as high as 110 pm/V (compared to ∼50 pm/V for thin-film rhombohedral BFO) and dramatic increases in the out-of-plane dielectric constant (ε_{33}) up to 400 (compared with ∼150 in thin-film BFO). Such findings have been supported by high-resolution crystallographic studies [21] which established the coexistence of the polar and nonpolar phases across a substantial range of temperatures and thicknesses as well as atomic-scale modulation of the polar phase due to a flexoelectric interaction [22–25].

Given the immense interest in RE-doped BFO thin films as a suitable environmentally friendly lead- (Pb-) free piezoelectric, we thus investigated the feasibility of implementing electrostatic and strain-coupling techniques previously exploited for PbTiO$_3$-based systems [26] to tuning the polar-to-nonpolar phase transition. However, we approach this from a different angle: We ask if it is possible to change the chemical composition at which a polar phase transformation occurs by controlling the strength of the interlayer interactions in the superlattice for constant average compositions. Interface control of a MPB transition and resultant functional behavior in (001)-oriented epitaxial BiFeO$_3$/(Bi$_{1-x}$Sm$_x$)FeO$_3$ multilayers thus forms the key motivation of this paper.

We show that changing the individual layer thickness in superlattices alters the interlayer strain and polarization coupling between the BFO and the Bi$_x$Sm$_{(1-x)}$FeO$_3$ (BSFO) layers (even though the average composition remains constant), and therefore the resultant phase stabilizes. We demonstrate these findings by employing composition-spread growth of 200 nm (in overall thickness) BiFeO$_3$/(Bi$_{1-x}$Sm$_x$)FeO$_3$ epitaxial thin-film superlattices. For short period superlattices, we show that the strength of interlaying polar coupling increases (as confirmed by mean-field Landau-Ginzburg-Devonshire computations) and acts as a mechanism to stabilize the incommensurately modulated phase (MP) in BSFO [23]. As a consequence, a large switchable polarization is found even for BiFeO$_3$/(Bi$_{1-x}$Sm$_x$)FeO$_3$ multilayers whose average Sm^{3+} compositions were previously established to be paraelectric in single-layer films. Concomitant with these structural and polar changes, a large enhancement in dielectric behavior is observed. Increasing the layer thickness results (ultimately) to a point where this in-plane coupling is lost and observed behavior reverts to those previously observed for single-layer films.

We focused on tunability of phase transition near the MPB composition. For this reason, we selected BFO and BSFO as our two components of the superlattice. The composition-spread scheme is implemented in such a way so that the overall superlattice structure is maintained across the spread chip, but alternate layers (BSFO) have the composition varying from BFO to (Bi$_{0.75}$Sm$_{0.25}$)FeO$_3$.

II. EXPERIMENTAL METHODS

Combinatorial pulsed laser deposition was used to fabricate composition spreads of 200-nm [BiFeO$_3$/Bi$_{1-x}$Sm$_x$FeO$_3$] multilayers on SrRuO$_3$ buffer layers. For each film, a composition spread with a gradient from $x = 0$ to $x = 0.3$ across an 8-mm length of the substrates is obtained. Ceramic targets of Bi$_{1.1}$FeO$_3$ and SmFeO$_3$ were ablated with a KrF excimer laser ($\lambda = 248$ nm thin-film star). Temperatures of 630 °C, 100-mT O$_2$ partial pressure, laser fluence of 0.8 J/cm^2, and laser pulse frequency of 5 Hz were used to grow the SrRuO$_3$ bottom electrode to a total thickness of 50 nm. [BiFeO$_3$/(Bi$_{1-x}$Sm$_x$)FeO$_3$] multilayers were grown at 590 °C, 25-mT oxygen partial pressure, 0.8-J/cm^2 laser fluence, and 40-Hz laser pulse frequency. The thickness of each layer varies between 5 and 50 nm per layer, and all samples were grown to a total thickness of 200 nm. The compositions across the combinatorial spread multilayers were probed using an electron probe (JEOL JXA-8900, Japan) with a variance of ±1% at each measurement point. X-ray diffraction (XRD) measurements were taken using a conventional four-circle x-ray diffractometer (PANalytical X-Pert MRD, Germany) and a two-dimensional x-ray diffraction (2DXRD) (Bruker D8 Discover with Bruker general area detector diffraction system (GADDS)). Electrical characterization was facilitated through the growth and patterning via the lift-off process of 50×50×0.1-μm Pd top electrodes in addition to physically masked circular 100 × 0.1- and 200×0.1-μm Pt electrodes grown via electron-beam deposition. Polarization-electric-field measurements were measured at 50 kHz using a radiant multiferroic loop analyzer. Dielectric properties were measured using an LCR meter (HP 4194A) using an ac signal of 80 mV and 100 kHz and a custom cold-stage measurement station set to a temperature of 200 K at a chamber base pressure of ∼5e^{-5} Torr [27].

III. RESULTS AND DISCUSSION

It is important to first understand the difference between the present superlattices and our previous paper on non-superlattice composition-spread studies [3,15,16]. Figure 1(a) is a schematic of BFO/BSFO multilayers investigated here, and Fig. 1(b) shows a schematic of the single-layer BSFO combinatorial spread thin film investigated previously. We have fabricated four superlattice composition spreads. The overall thickness for all four systems is fixed at 200 nm. We use the nomenclature $[h/h]_m$, where h is the layer thickness and m is the number of layers of each component. Four sets of [BiFeO$_3$/(Bi$_{1-x}$Sm$_x$)FeO$_3$] multilayer samples had individual layer thicknesses h of 5-nm [5/5]$_{20}$, 10-nm [10/10]$_{10}$, 20-nm [20/20]$_5$, and 50-nm [50/50]$_2$ periodicities. Each Bi$_{1-x}$Sm$_x$FeO$_3$ layer was deposited in such a way so that it is a composition spread in the lateral direction across the sample as shown in Fig. 1(a). In the thickness direction, the average composition for all four samples at any given location across the stack is the same. That is, on a macroscale, each sample is (BiFeO$_3$)$_{0.5}$/[(Bi$_{1-x}$Sm$_x$)FeO$_3$]$_{0.5}$. This is important— it ensures that any fundamental composition-driven effects would affect all samples equally and conversely and any differences can be purely attributed to the interlayer coupling mechanisms.
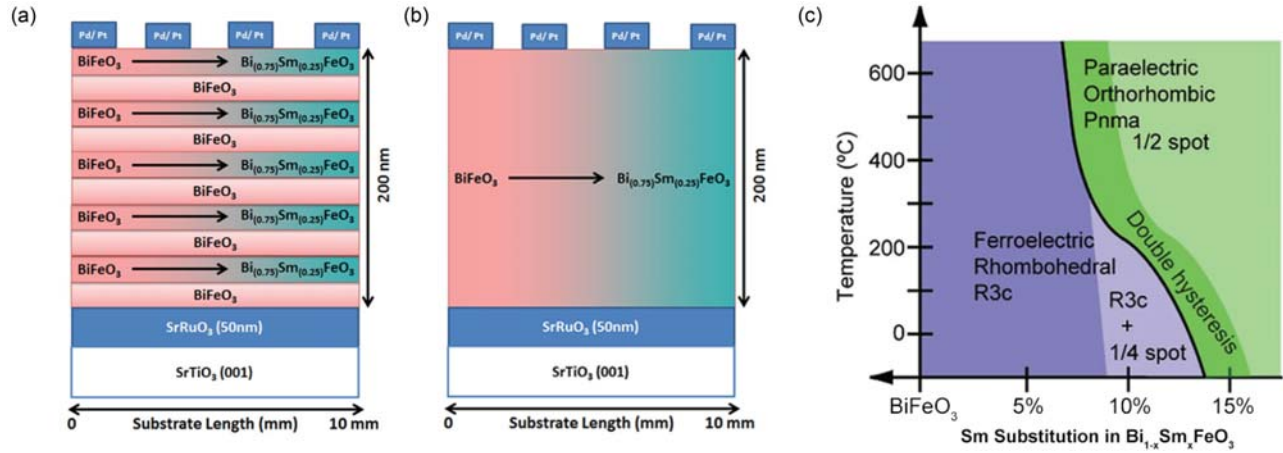
FIG. 1. (Color online) Cross-sectional schematics of the (a) $[20/20]_5$ $BiFeO_3/Bi_{(1-x)}Sm_{(x)}FeO_3$ multilayers and (b) single-layer $Bi_{(1-x)}Sm_{(x)}FeO_3$ thin film, illustrating the compositional gradient of increasing Sm substitution across the length of the substrate. (c) Phase diagram from Kan *et al.* [18] showing the structural transitions among the $R3c$, $Pbam$, and $Pnma$ phases across single layer $Bi_{(1-x)}Sm_{(x)}FeO_3$.

Prior to any discussion related to either structural or polar properties it is instructive to refresh the complex sequence of phase transitions and the evolution of polar properties as a function of Sm^{3+} doping found for single-layer BSFO. Figure 1(c) is a phase diagram adapted from prior work by Kan *et al.* [18] and Borisevich *et al.* [23]. Briefly, for Sm^{3+} concentrations up to 6% no notable changes in the $R3c$ structure or polarization properties are observed with both x-ray diffraction and selective area electron diffraction (SAED) showing simply the fundamental perovskite peaks. When the concentration of Sm^{3+} is increased beyond 6%, the addition of Sm^{3+} dramatically modifies the local dipole alignments, creating pockets of a $PbZrO_3$-(PZO-) like $Pbam$ phase with antiparallel A-site cation displacement. Softening modes which give rise to local AFE phases in these pockets result in quadrupling of the unit cell along the $\langle 011 \rangle$ direction with dimensions of $\sqrt{2}a \times 2\sqrt{2}a \times 2a$, where a is the lattice parameter of the pseudocubic perovskite unit cell, which results in their 2DXRD and SAED patterns showing the so-called $\frac{1}{4}\{011\}$ superstructure spots. Hereafter this is simply referred to as the "$\frac{1}{4}$ spot." This phase has also been identified by Kalantari *et al.* in Nd-doped BFO [28]. From a polar perspective, the P-E loops show a very square nature, improved saturation, and reduced coercive field.

As more Sm^{3+} is added, the clusters of the AFE regions expand within a FE matrix, and at the critical concentration of $x = 0.14$, sufficient chemical pressure from the Sm^{3+} addition results in an incommensuration phenomenon where the system adopts a complex nanoscale mixture bridging between Bi-rich rhombohedral and Sm-rich orthorhombic phases. We found that the BSFO system adapts itself as a compromise between displacement of cations related quadrupling of the unit cell for $x < 0.14$ and rotation of oxygen related doubling of the unit cell for $x > 0.14$ in a manner favoring nanoscale phase coexistence and giving rise to the incommensurately modulated bridging phase. This phase has a very complex diffraction signature [23,29], and it shows both a $\frac{1}{4}$ spot from the antiparallel A-site cation displacement and a $\frac{1}{2}$ (010) superstructure from the cell-doubled Sm-orthoferrite phase.

From this juncture onward, for concentrations of Sm^{3+} up to 17% the P-E loops progressively change from a square hysteresis to a double hysteresis, signifying the onset of the field-induced $O \rightarrow R$ phase transition.

For Sm^{3+} concentrations beyond 17%, the antiparallel cation displacement component totally vanishes as signified by the disappearance of the $\frac{1}{4}\{011\}$ spots. Instead, the cell-doubled orthorhombic $Pnma$ phase gains increasing stability with the distinctive $\frac{1}{2}$ (010) superstructure spots observed in the 2DXRD and SAED patterns. This is the so-called "$\frac{1}{2}$ spot." Here the polar character of the system completely disappears, and a paraelectric P-E loop is observed. We also note that for single-layer compositions beyond 17%, a substantive jump in the dielectric leakage is found as evidenced by extremely high loss values.

Table I outlines the key features of each crystallographic phase in terms of its structural and polar signature.

With this background in mind, this paper starts with x-ray diffraction analysis of the synthesized superlattices. Figure 2(a) shows the θ-2θ scan series acquired around the (001) $SrTiO_3$ Bragg reflection for $[5/5]_{20}$, $[10/10]_{10}$, and $[50/50]_2$ samples, respectively. The 20-nm $[20/20]_5$ data are shown with the supplementary datasets where full range scans ($2\theta = 20-80$) are also provided in the Supplemental Material S1 [30]. The compositions refer to the percentage of Sm^{3+} in the BSFO layer. Observing the BFO compositions for the multilayers, only a single (001) pseudocubic $BiFeO_3$ phase is observed, demonstrating the phase-pure and fully c-axis-oriented nature of the BFO thin-film growth.

For all three samples, as Sm^{3+} content in the multilayer is increased, the major (001) reflection shifts towards higher 2θ, in line with previous observations for the monolithic Sm^{3+}-doped BFO thin films [21,29]. However, the extent of this 2θ shift varies depending on periodicity.

The emergence of the satellite peaks (indicated with an *) present in the $[5/5]_{20}$ and $[10/10]_{10}$ multilayers at compositions beyond 6% Sm^{3+} content imply the onset of a superstructure with a period related to the thickness of the multilayers. Indeed, calculations of the spacing of the satellite

TABLE I. Structural features of $Bi_{1-x}Sm_xFeO_3$ thin films as a function of Sm^{3+} substitution [18,19,21,26,29,32].

| $Bi_xSm_{1-x}FeO_3$−Sm content	Crystallographic features	P-E hysteresis character
<6%	Rhombohedral $R3c$	Square P-E loops
6%−12%	$R3c + \frac{1}{4}\{011\}$ superstructure, pockets of antipolar PZO-like phase	Square P-E loops with reduced leakage
12%−14%	Incommensurately modulated phase with coexistence of pockets of $R3c + \frac{1}{4}\{011\}$ and pockets of an orthorhombic cell doubled $\frac{1}{2}\{010\}$ superstructure	Onset of double hysteresis. P-E loop appears pinched.
14%−17%	Morphotropic phase boundary with an increasing orthorhombic cell doubled $\frac{1}{2}\{010\}$ superstructure	Double hysteresis P-E loop
>17%	Only an orthorhombic cell doubled phase with a $\frac{1}{2}\{010\}$ superstructure	Nonpolar paraelectric P-E loop
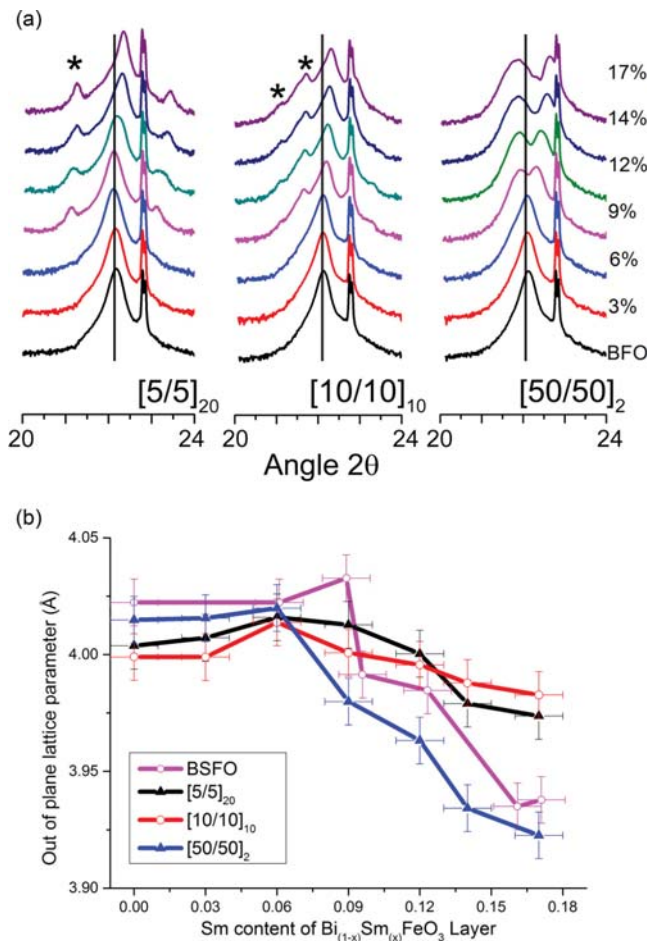
FIG. 2. (Color online) (a) High-resolution x-ray diffraction mapping of the crystallographic evolution of the $BiFeO_3/Bi_{(1-x)}Sm_{(x)}FeO_3$ multilayers with periodicity. The * locations indicate observations of satellite peaks associated with the periodic nature of the multilayers, and the vertical lines are a visual guide to the change in main peak displacement relative to the BFO(001) peak. (b) Calculated d spacings of the $Bi_{(1-x)}Sm_{(x)}FeO_3$ (001) peak as a function of Sm^{3+} content and multilayer periodicity, compared with single-layer BSFO thin films from previous research [18]. The out-of-plane periodicity is calculated with $\Lambda = ld_{001}$.

peaks from the major thin-film peaks using the formula $d = \lambda/2(\sin\theta_{n+1} - \sin\theta_n)$ [26] indicate that this can be attributed to the interval between the multilayers and correspond to the $[5/5]_{20}$ and $[10/10]_{10}$ periodicities. Thus in the $[5/5]_{20}$ and $[10/10]_{10}$ multilayers, the presence of a single main c-axis peak along with satellites indicates that the strain between the individual layers is translated through the thickness of the entire stack and hence in-plane coherency is fully maintained.

On the other hand no such satellite peaks are observed for the $[50/50]_2$ sample. Instead the $[50/50]_2$ multilayers exhibit a gradual peak broadening with increasing Sm^{3+} concentrations up to 9%. Up to 9% the changes in the lattice parameter as a result of Sm^{3+} doping are relatively small such that the resultant strain is seemingly accommodated by the thick layers. Beyond 9% we observe the onset of a peak splitting. The position of this second peak ($2\theta = 22.330$, $d = 0.3980$ nm) along with the detailed 2DXRD scans (discussed next) indicates the formation of the orthoferrite phase with its long axis (b axis) now normal to the in-plane direction. The splitting becomes stronger as more Sm^{3+} is added where two fully separated main peaks emerge beyond 12% Sm. The extent of the peak splitting increases beyond 14%Sm^{3+}, which is the MPB composition for single-layer films. This indicates that the BFO and BSFO layers are no longer coupled to each other and behave independently of each other. This is a thickness effect where the thickness of each individual layer (50 nm) is now too thick to maintain any level of interlayer coupling.

Figure 2(b) plots the out-of-plane lattice parameter for the (001) peak position. The $[5/5]_{20}$ and $[10/10]_{10}$ multilayers reveal a very gradual decrease from 0.4 to 0.397 nm in $[5/5]_{20}$ and 0.4 to 0.398 nm in $[10/10]_{10}$ in the lattice parameter through the measured compositional range. On the other hand a sharp drop in lattice parameter is observed in the $[50/50]_2$ film, much like the single-layer BSFO system. We emphasize that this lattice parameter trend bears a very close relationship with the $R \rightarrow O$ phase transition where a massive volume collapse is associated with the $R \rightarrow O$ phase transition [21,29]. The lack of such a collapse in the short period samples hints that the two layers are coupled such that the $R \rightarrow O$ phase transition is suppressed unlike in the $[50/50]_2$ sample.

Reciprocal space maps (Supplemental Material S2 [30]) acquired around the (103) axis confirm not only the epitaxial nature of the samples, but also the presence of only a single
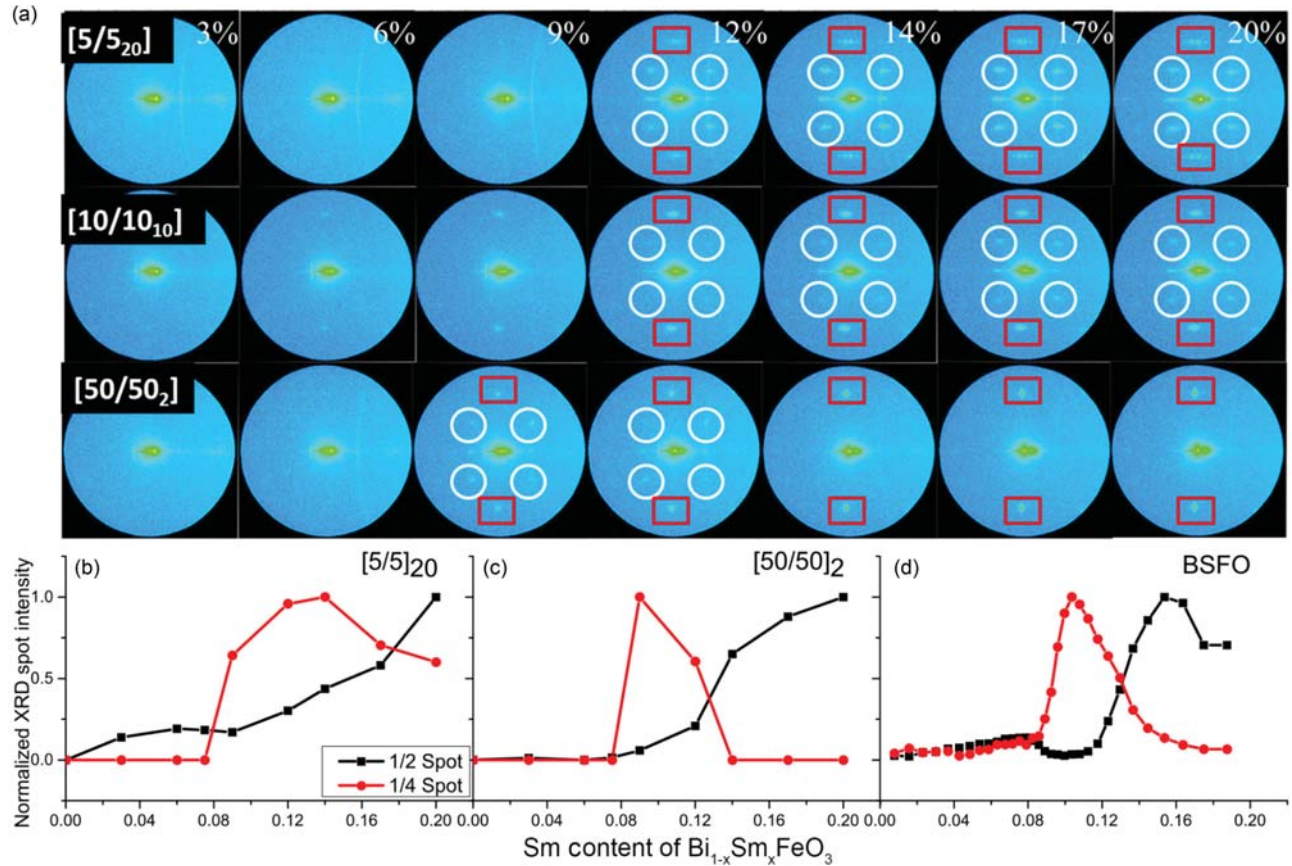
FIG. 3. (Color online) (a) Two-dimensional XRD maps of $\langle 002 \rangle$ reflection of $BiFeO_3/Bi_{(1-x)}Sm_{(x)}FeO_3$ multilayers with periodicity of 5–50 nm. The white circles and red squares denote the $\frac{1}{4}$ {011} spot superstructure and the $\frac{1}{2}$ {010} superstructure peaks, respectively. By reducing the thickness of each layer, the $\frac{1}{4}$ {011} spot associated with the ferroelectric $R3c$ phase is stabilized at compositions of the $Bi_{(1-x)}Sm_{(x)}FeO_3$ layer considered to be O phase in single-layer BSFO. This is observed in the $[5/5]_{20}$ and $[10/10]_{10}$ multilayers but not in the $[50/50]_2$ multilayer. (b) Satellite peak intensity comparisons of the $[5/5]_{20}$, $[50/50]_2$ superlattices, and single-layer BSFO (400-nm thickness) from previous research [18]. The decay of the $\frac{1}{4}$ spot peak is shifted to higher compositions by moving from single-layer BSFO to the highly periodic $[5/5]_{20}$ multilayers, which is normally correlated to the onset of the structural phase transition from $R \rightarrow O$ BSFO.

peak in the $[5/5]_{20}$ sample. The lack of a peak splitting confirms that: (i) The layers are acting in a coupled fashion corresponding to a singular superlattice composed of BFO and BSFO layers and (ii) that the unit cells do not have reduced symmetry. In other words the presence of either a bridging phase with lower symmetry, akin to that observed in Ref. [31], or polarization rotation [17] can be precluded. The thicker $[50/50]_2$ sample shows a weak peak split. Analysis of the q vectors confirms this corresponds to the decoupling of the two layers and not from any polarization rotation.

Figure 3(a) shows 2DXRD images taken around the $SrTiO_3$ (STO) (002) reflection and captures the structural evolution of the $[BiFeO_3/(Bi_{1-x}Sm_x)FeO_3]$ multilayers as a function of Sm^{3+} content and periodicity. Intensities of both the $\frac{1}{4}$ and the $\frac{1}{2}$ superstructure spots (see Supplemental Material S3 [30] for cross-sectional profiles) are shown in Figs. 3(b)–3(d) for the $[5/5]_{20}$, $[50/50]_2$, and single-layer BSFO (taken from Kan *et al.* [18]), respectively.

The figure shows in the $[5/5]_{20}$ and $[10/10]_{10}$ multilayers, the $\frac{1}{4}$ spots persist in Sm^{3+} concentrations much higher than their range of stability (up to 14%) for the single layer and the $[50/50]_2$ multilayer. Again, in contrast to the short

period samples the $[50/50]_2$ sample follows an emergence and disappearance of the $\frac{1}{4}$ spot equivalent to that of single-layer BSFO compositions. This is most strongly exemplified beyond the 17% Sm^{3+} concentration where the $\frac{1}{4}$ and $\frac{1}{2}$ spots in the $[5/5]_{20}$ and $[10/10]_{10}$ samples are clearly visible, but in the $[50/50]_2$ sample only the $\frac{1}{2}$ spot associated with the orthorhombic phase is present. The normal θ-2θ scans in conjunction with 2DXRD area scans thus indicate that the region of stability of the incommensurately modulated phase in these short period ($[5/5]_{20}$ and $[10/10]_{10}$) superlattice samples has been expanded to higher Sm^{3+} concentrations, attributed below to the strength of short-range coupling.

Figure 4 displays the ferroelectric hysteresis (P-E) loops for the $[5/5]_{20}$, $[10/10]_{10}$, and $[50/50]_2$ multilayers at room temperature. (A full set with the $[20/20]_5$ data is shown in the Supplemental Material S4 [30]). Generally at Sm^{3+} concentrations up to 6%, only a minor variation in the remnant polarization (P_r) is observed as a function of multilayer periodicity, in line with the XRD trends. Second, overall the measured P_r monotonically decreases with increasing layer thickness for a given composition. The origin of this behavior is discussed later via Landau-Ginzburg-Devonshire analysis
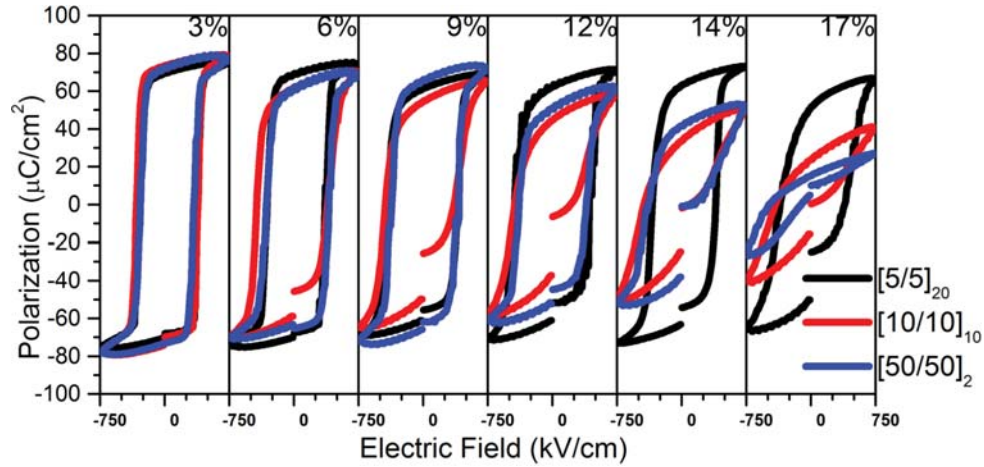
FIG. 4. (Color online) P-E hysteresis loops of $BiFeO_3/Bi_{(1-x)}Sm_{(x)}FeO_3$ multilayers, showing the tuning of the ferroelectric character of the multilayers with layer thickness and Sm^{3+} content of the $Bi_{(1-x)}Sm_{(x)}FeO_3$ layer. At $x = 0.17$, the highly periodic $[5/5]_{20}$ and $[10/10]_{10}$ multilayers exhibit a restoration of the ferroelectric character, consistent with the crystallographic measurements indicating the $R3c + \frac{1}{4}\{011\}$ superstructure ferroelectric phase.

of the superlattices. Distinct changes between the $[5/5]_{20}$ and the $[50/50]_2$ multilayers become immediately evident with the trends for the $[10/10]_{10}$ and $[20/20]_5$ samples falling between the two extremes. For the $[5/5]_{20}$ sample, a very small change in the remnant polarization is observed (Supplemental Material S5 [30]), and in fact even at 14% Sm^{3+} a reduction in P_r is not observed. In comparison, the polarization begins to rapidly drop at and beyond 14% Sm^{3+} for the $[50/50]_2$ and single-layer Sm^{3+}-doped BFO thin films. In fact the $[5/5]_{20}$ films continue to display a strong ferroelectric character (evidenced by the square loops), even up to the measured 17% Sm^{3+} content.

These observations can be easily explained by the XRD data. Recall that the presence of each type of superstructure peak bears a deep relationship with the ultimate polar behavior observed for single-layer RE-doped BFO films. For example, the onset of the $Pbam$ phase with $\frac{1}{4}\{011\}$ peaks has been previously shown to improve polarization hysteresis behavior [17–19] whereas the presence of an incommensurate phase mixture (both $\frac{1}{2}(010)$ and $\frac{1}{4}\{011\}$ spots) is a necessity for enhanced electromechanical response [17–19]. Finally, the presence of only $Pnma$ with $\frac{1}{2}\{010\}$ peaks indicates the formation of the paraelectric orthoferrite phase [18,19,31].

As the thickness of the multilayers decreases from $[50/50]_2$ to $[5/5]_{20}$, the composition space over which a phase mixture with both $\frac{1}{4}$ and $\frac{1}{2}$ spots is observed is extended whereas the appearance of sole $\frac{1}{2}\{010\}$ superstructure spots (that corresponds to the rare-earth $Pnma$ orthoferrite paraelectric phase) is hindered. Therefore, even at compositions where single-layer BSFO thin films were shown to undergo a polar $Pbam \rightarrow$ nonpolar $Pnma$ transition, the imposed superlattice coupling stabilizes a global ferroelectric polar state. For the thicker $[20/20]_5$ and $[50/50]_2$ samples where interlayer coupling is weak, the system behaves much like two independent layers. Now the paraelectric phase dominates the P-E behavior thus resulting in a rapid decay in remnant polarization.

At the outset this could simply be interpreted as an in-plane strain effect. However, we note that, although the strain

states (lattice parameter data) for $[5/5]_{20}$ and $[10/10]_{10}$ are practically identical (within experimental error), the observed polarization behavior is markedly different where the drop in P_r for the $[10/10]_{10}$ sample is more drastic compared to the $[5/5]_{20}$ sample. Previous reports for $PbTiO_3$ (PTO)/STO [32] and $BaTiO_3/CaTiO_3$/STO [4] have unambiguously shown that the polarization displacement continuity through the paraelectric layer is key to stabilization of a ferroelectric phase. We thus proceeded to check for the same here. Single-frequency piezoresponse force microscopy (PFM) images in both out-of-plane (OPPFM) and lateral in-plane (LPFM) were acquired as a function of Sm^{3+} concentration for each system as shown in Fig. 5. Care was taken to ensure any changes observed could be solely attributed to polar properties of the films imaged as opposed to tip wear.

First with increasing Sm^{3+}, the LPFM contrast begins to weaken, irrespective of layer thickness. PFM investigations previously carried out for the Sm-doped BFO samples found that the polar phase transition stems from the rotation of the polarization rotation vector from the $\langle 111 \rangle$ to the $\langle 001 \rangle$ direction as a function of Sm^{3+} substitution [22], and this could explain the gradual weakening of the LPFM response. However the most distinct changes occur for the OPPFM images. For example, the $[5/5]_{20}$ system shows a strong fully out-of-plane response (coupled with a very weak in-plane response) for 17% Sm^{3+}, indicative of only c-axis-oriented domains. The presence of both dark and white contrasts in the OPPFM images shows both positive and negative orientations of the c domains exist in the as-grown state. In contrast, the $[50/50]_2$ sample shows zero signal (brown contrast) for this composition, in agreement with the lack of any P_r as found in Fig. 4. There is also a systematic decay in the strength of this OPPFM response with increasing Sm^{3+} as the layer thickness increases. The PFM images, along with the XRD and P-E data suggest that, although there is a rotation caused by Sm^{3+} substitution to the (001) direction, the phase transition to the nonpolar orthorhombic phase is restricted for the short period superlattices.
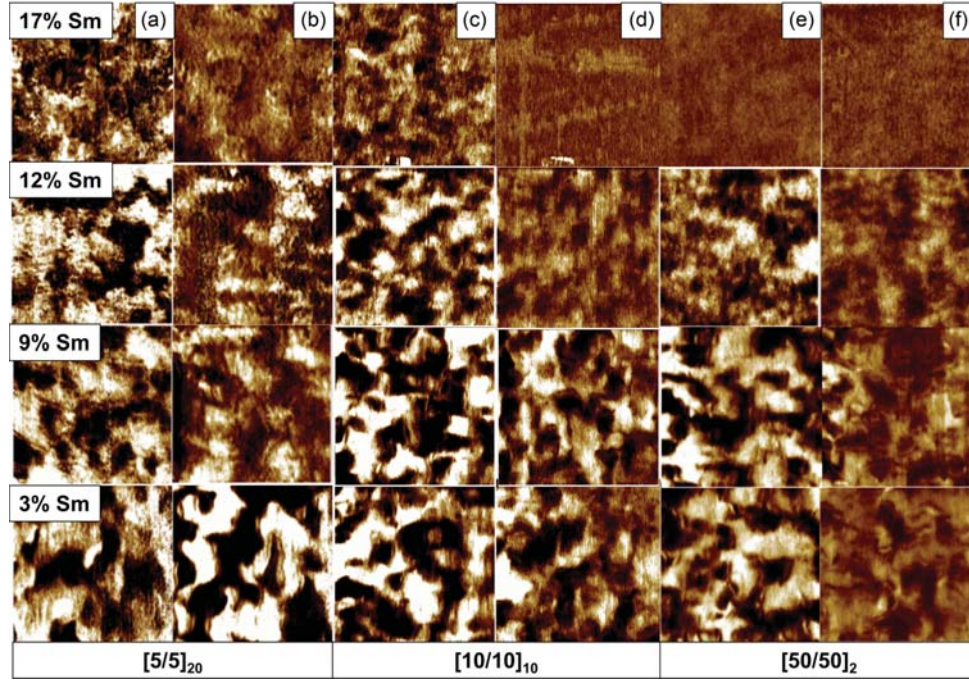
FIG. 5. (Color online) Ferroelectric domain evolution of BFO/BSFO Multilayers as a function of composition and multilayer periodicity, showing $2\mu m^2$ Out-of-Plane (a,c,e) and In-plane (b,d,f) PFM Maps of $BiFeO_3/Bi_{(1-x)}Sm_{(x)}FeO_3$ multilayers of $[5/5]_{20}$ (a,b), $[10/10]_{10}$ (c,d) and $[50/50]_2$ (e,f) thickness per layer. Out-of-plane domain contrast is observed at $x = 0.12/0.17$ in the $[5/5]_{20}$ and $[10/10]_{10}$ multilayers, but not in the $[50/50]_2$ multilayers, suggesting a restoration of ferroelectric domains with increased multilayer periodicity. All films exhibit fractal domain patterning, which can be attributed to the relatively high total thickness of the multilayers allowing for mitigation of strain effects from the substrate, in addition to the use of an exact (001) substrate rather than a vicinally cut substrate. As increasing Sm content is added, the polarization rotation vector for BSFO rotates in direction from $\langle 111 \rangle$ to $\langle 001 \rangle$, which should be observed as an increase in the out-of-plane PFM image contrast when the samples are grown epitaxially on (001) oriented substrates. With further substitution, the $R \rightarrow O$ phase transition results in the formation of the non-polar orthorhombic phase, which exhibits paraelectric character, and thus no ferroelectric domain contrast should be observed in either in-plane or out-of-plane PFM scans. In the $[5/5]_{20}$ and $[10/10]_{10}$ superlattices, an enhancement of out-of-plane PFM contrast is observed.

To understand if this is induced by the previously discussed polarization continuity requirement (that would emanate from the interspersed BFO layers), we performed a Landau-Ginzburg-Devonshire analysis. Full mathematical details are provided in Supplemental Material S6 [30], Appendix A). The thickness of the BFO layer was assumed to be h_1 whereas the thickness of the BSFO layer was assumed to be h_2. For the present analysis, each layer was assumed to be thin enough to be epitaxially strained by a thick rigid $SrTiO_3$ substrate with an electrode, so as to avoid complications from misfit dislocations. Hereinafter, (1) denotes BFO and (2) denotes BSFO values. In order to study the phase diagram of $Bi_xSm_{1-x}FeO_3$ multilayers, we consider only out-of-plane component of polarization P_3 and tilt vector Φ. Direct atomically resolved mapping of polarization and structure order parameter fields showed that to fully explain the phase diagram of this system, one needs to take into account the flexoelectric interaction at the phase boundary. The corresponding free-energy bulk density along with the flexoantiferrodistortive coupling [23,24] thus acquires the form

$$G = \frac{1}{h_1}\int_{-h_1}^{0}dz f^{(1)} + \frac{1}{h_2}\int_{0}^{h_2}dz f^{(2)} + G_I, \quad (1a)$$

where

$$f^{(i)} = \left[\frac{a_3^{(i)}(z,x)}{2}P_3^2 + \frac{a_{33}^{(i)}}{4}P_3^4 + \frac{g_{33}^{(i)}}{2}\left(\frac{\partial P_3}{\partial z}\right)^2 - \frac{P_3 E_3^d}{2} \right.$$
$$- \eta^{(i)}P_3^2\Phi^2 \frac{b_3^{(i)}(z,x)}{2}\Phi^2 + \frac{b_{33}^{(i)}}{4}\Phi^4 + \frac{v_{33}^{(i)}}{2}\left(\frac{\partial \Phi}{\partial z}\right)^2$$
$$\left. + \frac{\xi^{(i)}}{2}\left(\frac{\partial P_3}{\partial z}\Phi^2 - P_3\frac{\partial(\Phi^2)}{\partial z}\right) \right]. \quad (1b)$$

The strength of the flexoantiferrodistortive coupling is $\xi^{(i)}$, which can be renormalized by finite-size effects in thin films. Also the coupling coefficient can be renormalized by the rotoflexoelectric effect (product $F_{ijkl} \cdot r_{klmn}$) as $\xi_{ijmn}^{(i)} = \xi_\sigma^{(i)} + F_{ijkl} \cdot r_{klmn}$ [25,30,33].

Let us consider the polarization, tilt vector, and their derivatives to be continuous at the BFO/BSFO interface. For such a case the interface energy G_I can be omitted. For the sake of simplicity we further assume that $g_{33}^{(2)} = g_{33}^{(1)} = g$, $a_{33}^{(2)} = a_{33}^{(1)} = \alpha_{11}$, and $h_1 = h_2 = h$ and the background permittivity is the same for both BFO and BSFO. Using the results of
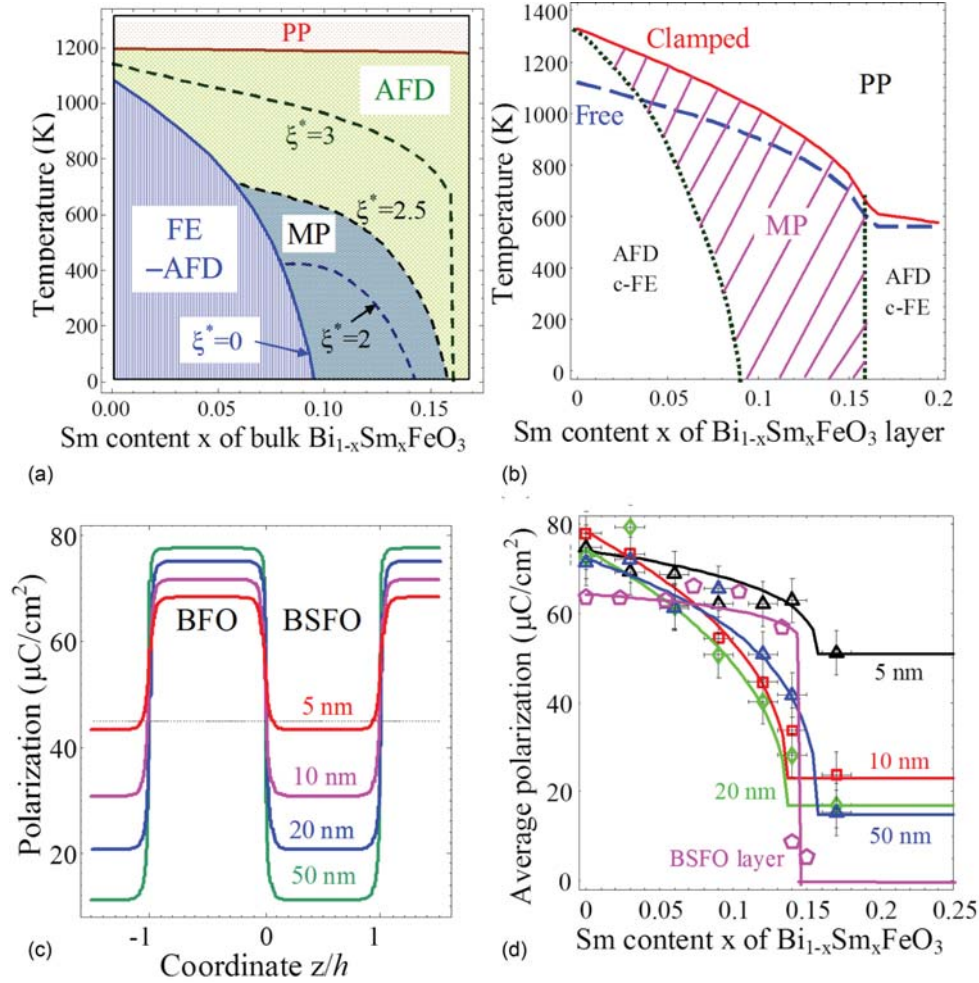
FIG. 6. (Color online) (a) Phase diagram of the bulk $Bi_x Sm_{1-x} FeO_3$ in coordinates temperature T-composition y calculated with an increase in the coupling term ξ^*. Values of the dimensionless coupling parameter $\xi^* = 0, 2, 2.5, 3$. (b) Phase diagrams of the BFO/BSFO multilayer in coordinates temperature T vs composition x for either clamped-on $SrTiO_3$ substrate (solid curve) or free standing (dashed curve). Note that the curves are almost the same for different half periods of multilayer $h_1 = h_2 = 50$, 10, and 5 nm. (c) Out-of-plane polarization profiles for $BiFeO_3/Bi_{0.8}Sm_{0.2}FeO_3$ multilayers with thickness $h = 5$, 10, 20, and 50 nm. The polarization and its gradient were regarded continuous at the BFO/BSFO interface. (d) Out-of-plane polarization component averaged over the BFO/BSFO multilayer period for different multilayer periods 5, 10, 20, 50, nm, and a single BSFO layer. Symbols are experimental data, and solid curves are the approximate formula (3) with the fitting parameters listed in Table S6.3 of the Supplemental Material.

Ref. [34] the corresponding depolarization field is

$$E_3^{(1)} = \frac{1}{\varepsilon_0 \varepsilon_b} \left[\frac{1}{2} \left(\langle P_3^{(1)} \rangle + \langle P_3^{(2)} \rangle \right) - P_3^{(1)} \right],$$

$$E_3^{(2)} = \frac{1}{\varepsilon_0 \varepsilon_b} \left[\frac{1}{2} \left(\langle P_3^{(1)} \rangle + \langle P_3^{(2)} \rangle \right) - P_3^{(2)} \right], \quad (2)$$

where $\langle P_3^{(i)} \rangle$ is the average polarization of each layer. The derivation for the approximate expression for the averaged polarization $\langle P_3 \rangle = \frac{1}{2}(\langle P_3^{(1)} \rangle + \langle P_3^{(2)} \rangle)$ can be found using the direct variational method [35–38],

$$\langle P_3 \rangle \approx P_r(h) + P_b(h) \sqrt{-\frac{T_C^{BFO}(1 - x/x_{cr})^\mu - T}{T_C^{BFO} - T}}, \quad (3)$$

where $P_r(h)$, $P_b(h)$, and power μ are fitting parameters. The analytical solution at $x = 0$ is trivial: $\langle P_3^{(1)} \rangle = \langle P_3^{(2)} \rangle = P_r +$

$P_b = P_b^{BFO}$. The material parameters used in the modeling correspond to the multilayer BFO/BSFO and are listed in Table S6.1 of the Supplemental Material [30,39–45].

We first present results for an infinitely thick slab (i.e., $h \to \infty$) as shown in Fig. 6(a) to simply illustrate the effect of the coupling parameter ξ^* where $\xi^* = |\xi^{(2)}|/(2\sqrt{v_{33}^{(2)}}\sqrt{a_{33}^{(2)} b_{33}^{(2)}})$.

There are four phases present in the phase diagram, namely, nonstructural paraelectric, antiferrodistortive, FE-antiferrodistortive, and an incommensurate MP. The shaded regions indicate MP absolute stability. One can see that the MP is absent for $\xi^* = 0$, but it appears with a nonzero (and positive) ξ^*, and its region of stability enlarges with increasing strength of ξ^*. The critical finding here is that the presence of the MP (the phase mixture) is not driven by the presence of a substrate.

This is further reinforced in Fig. 6(b) where the effect of a compressive STO substrate was taken into account

(see Supplemental Material S6 [30]). The calculations find that that phase diagram is practically independent of the presence of the substrate, other than the fact that the critical temperatures are much higher as the compressive $SrTiO_3$ substrate provides additional stability to the out-of-plane polarization phase (i.e., *c phase*) in the BFO/BSFO multilayer. This is a well-established idea and in agreement with calculations for other ferroelectric perovskites [38]. Figure 6(b) critically finds the temperature of transition between the paraelectric and the *c* phase depends mainly on the ratio h_1/h_2 with the depolarization field along the *c* axis determining the shift in transition temperature.

This is best illustrated in the computed *c*-phase polarization profiles for $BiFeO_3/Bi_{0.8}Sm_{0.2}FeO_3$ multilayers with $h_1 = h_2 = 50, 20, 10$, and 5 nm as shown in Fig. 6(c). The dependence of the average out-of-plane spontaneous polarization on the Sm^{3+} concentration x (at room temperature) is shown in Fig. 6(d). The solid curves in Fig. 6(d), calculated for a different layer period h, show that the average polarization monotonically decreases with increasing Sm^{3+} concentration irrespective of the layer period. The symbols in Fig. 6(d) are points acquired from experimental results. Thus the predictions of the mean-field model and the experimentally measured points agree remarkably well right to the critical point, denoted as x_{cr}. This corresponds to a scenario when the BSFO layer becomes paraelectric with the BFO layers inducing all its polarization. Since the critical concentration for the onset of the paraelectric phase (i.e., disappearance of the ferroelectric phase) in single-layer BSFO was found to be $x_{cr} \sim 0.15$ [19], the nonzero polarizations computed (and observed) for the higher Sm^{3+} concentrations must thus exist necessarily due to the interfacial interactions of the multilayer structure induced by the electric field emanating from the BFO ferroelectric layers. This field, whereas being depolarizing within the BFO layer, acts to polarize outside the BFO boundaries. The electric-field distribution across the layers computed by the mean-field theory is shown in Supplemental Material S6.4 [30].

Having thus understood the origin of this interface effect, we next examined the dielectric susceptibilities as typically they are most sensitive to presence (or absence) of a phase boundary. In the single-layer BSFO thin-film system, compositions straddling the $R \to O$ phase-transition boundary exhibit a unique signature in their capacitance-voltage (*C*-*V*) behavior [18,21,29,31]. Namely, the *C*-*V* loops show a double-butterfly-shaped loop, indicated by the presence of four humps. This is attributed to the electric-field-induced phase transition, which also results in a double-hysteretic *P*-*E* loop [18]. This suggests that at compositions at or slightly beyond the $R \to O$ phase transition in BSFO, the presence of the quadrupled capacitance-voltage curves would indicate the occurrence of the $R \to O$ phase transition. In Fig. 7, capacitance-voltage curves are measured at a temperature of 200 K as a function of composition and multilayer periodicity. A temperature of 200 K was chosen to minimize the effect of leakage currents from the $BiFeO_3$ and BSFO layers. The dielectric constant (ε_{33}) was calculated using the parallel-plate capacitor model at zero-bias offset (tan δ plots are provided in Supplemental Material S7 [30]). Based on Figs. 2–4, which revealed the physically coupled nature of the $[5/5]_{20}$ and
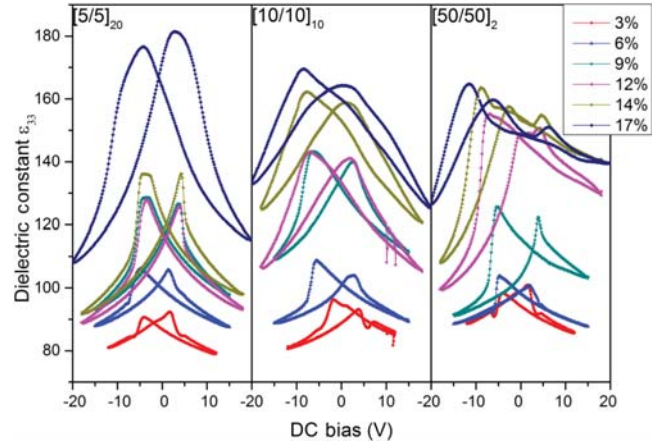

FIG. 7. (Color online) Cold-stage capacitance-voltage measurements taken at 200 K/100 kHz with a HP4194A LCR meter, demonstrating a notable increase in dielectric constant with increasing $BiFeO_3/Bi_{(1-x)}Sm_{(x)}FeO_3$ multilayer periodicity at $x = 0.17$ in $Bi_{(1-x)}Sm_{(x)}FeO_3$.

$[10/10]_{10}$ layers, the quadruple-humped capacitance-voltage curves are not expected. This is due to the suppression of the $R \to O$ phase transition for the BSFO layer. Conversely, the $[50/50]_2$ superlattices should respond to the application of dc bias by undergoing an $R \to O$ phase transition and result in the observation of quadruple-humped loops due to the lack of any physical coupling.

Figure 7 confirms the above hypothesis. Although both the $[5/5]_{20}$ and the $[10/10]_{10}$ samples display a marked increase in the observed out-of-plane dielectric constant at Sm^{3+} content above 17%, the key difference lies in the dielectric behavior of compositions beyond 12% Sm^{3+}. First, the maximum observed dielectric constant continues to monotonically increase for the $[5/5]_{20}$ and $[10/10]_{10}$ multilayers up to 17% Sm^{3+} content, increasing to a maximum of ~170 in the $[5/5]_{20}$ sample. The lack of quadruple humps for the $[5/5]_{20}$ sample for compositions beyond 12% correlate well with the *P*-*E* and PFM results in Figs. 4 and 5, respectively. That is, the BSFO layers are fully polarized in the out-of-plane direction for Sm compositions beyond the single-layer MPB. On the other hand a broadening of peaks is observed for the $[10/10]_{10}$ sample. A closer look at the 14% and 17% samples reveals that the broadening may stem from the onset of a field-induced phase transition with a fine shoulder being visible for these two compositions. This becomes evidently clear for $[50/50]_2$. In stark contrast to the short period samples, a clear double-hysteretic *C*-*V* loop (with four peaks) is observed for compositions beyond 12% Sm^{3+}, thus signifying the onset of a field-induced $O \to R$ phase transition. Figure 8 plots the dielectric constant at zero bias in comparison to single-layer BSFO thin films [18]. Whereas the short period superlattice demonstrates a monotonic increase in the dielectric constant (up to 17% Sm^{3+}), both the thicker $[50/50]_2$ and the single-layer BSFO thin films show a maximum dielectric constant at 14% Sm^{3+} followed by a drop. This shift in the peak in the short period superlattices to the right suggests that the phase boundary for the $[5/5]_{20}$ and $[10/10]_{10}$ superlattices is shifting to a higher Sm^{3+} content in agreement with the structural and
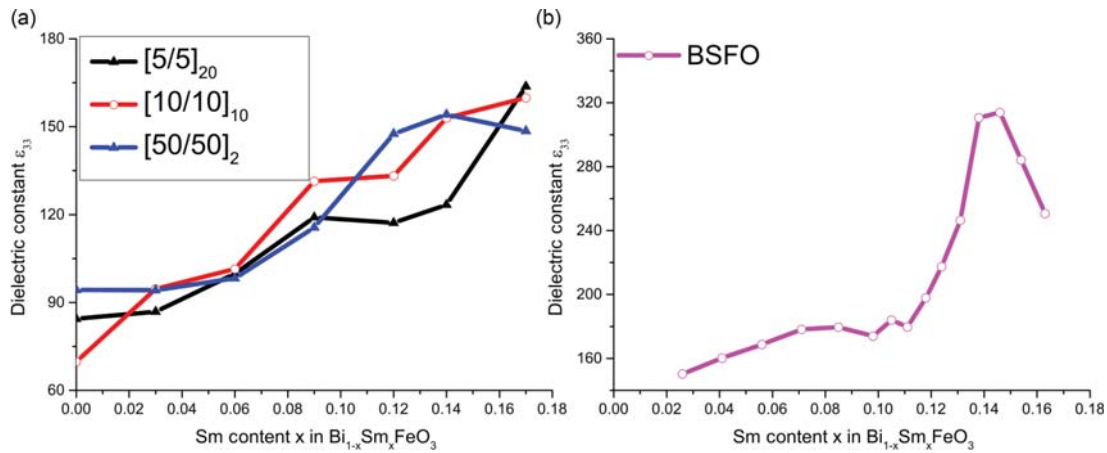
FIG. 8. (Color online) Dielectric constant ε_{33} at 200 K/100 kHz as a function of Sm^{3+} content and periodicity compared to the single-layer BSFO thin films [21,29]. Note that the measurement temperature of the single-layer BSFO thin films from literature is 293 K and was used due to an absence of measured data for single-layer BSFO thin films at temperatures of 200 K.

P-E measurements. Although measurements were carried out for concentrations higher than 17% Sm^{3+}, a sharp rise in the dielectric leakage precluded any reliable conclusions.

IV. CONCLUSION

To summarize, we show control of the FE(R) → PE(O) phase transition in epitaxial (001) $BiFeO_3/(Bi_{1-x}Sm_x)FeO_3$ 200-nm-thick superlattices ($0 \leqslant x \leqslant 0.25$) prepared by combinatorial PLD. Four sets of combinatorial spread BFO/BSFO samples, namely, $[5/5]_{20}$, $[10/10]_{10}$, $[20/20]_5$, and $[50/50]_2$ where $[h/h]_m$ means h is the layer thickness and m is the number of layers of each component were grown on $SrRuO_3$-buffered STO substrates. It is found the Sm^{3+} concentration required to drive the onset of the above phase transition is found to depend on the superlattice period (i.e., individual layer thickness), although the average composition for all superlattices investigated remained constant. As the layer thickness controls the strength of the interfacial coupling, modulation of the layer thickness affects the interfacial coupling. For short period superlattices (5- and 10-nm-thick individual layers), the thin films behave as a single coupled system with clear satellite peaks recorded in the XRD spectra. Additionally, 2DXRD maps find that the incommensurate MP (with signature "$R3c + \frac{1}{4}$ spot $+ \frac{1}{2}$ spot") stabilizes over a much larger Sm^{3+} concentration space, even as high as 17% Sm^{3+} (which is truly a nonpolar O PE phase in single-layer BSFO). Consequently these samples display robust square and saturated ferroelectric hysteresis loops, butterfly-shaped C-V curves, and strong domain contrast in the PFM images for the highest Sm^{3+} concentrations studied here. In contrast for the longer period

samples, beginning with the $[20/20]_5$ system, the interfacial coupling between the individual BFO and the BSFO layers begins to weaken such that $[50/50]_2$ multilayers are simply fully decoupled layers of $BiFeO_3$ and BSFO just stacked one on top of the other. The behavior then reverts broadly back to that of the single-layer BSFO system where above and beyond 14% Sm^{3+} a rapid degradation in the P-E hysteresis loops was observed. However unlike in previous papers [18,29], no field-induced double-hysteretic P-E loops were observed. Mean-field Landau theory confirms that the strength of the interface coupling controls the stability region of the incommensurate modulated phase and that the high remnant polarization values measured for the short period superlattices stem from an induced polarization by the BFO layers. The broader range of compositions where the modulated phase is observed in the highly periodic multilayers also suggests that this coupling can be utilized to increase the range of A-site substitution compositions which will result in the presence of the phase and thereby increase this window of enhanced electrical properties. As a large number of ferroelectric materials utilize narrow MPB compositions to yield improvements in their polar and electromechanical properties, this paper sheds further light on synthesis routes for artificially made MPB-like materials.

ACKNOWLEDGEMENTS

[1] H. W. Jang, D. A. Felker, C. W. Bark, Y. Wang, M. K. Niranjan, C. T. Nelson, Y. Zhang, D. Su, C. M. Folkman, S. H. Baek, S. Lee, K. Janicka, Y. Zhu, X. Q. Pan, D. D. Fong, E. Y. Tsymbal, M. S. Rzchowski, and C. B. Eom, Science **331**, 886 (2011).

[2] A. Ohtomo, D. Muller, J. Grazul, and H. Hwang, Nature (London) **419**, 378 (2002).

[3] E. Bousquet, M. Dawber, N. Stucki, C. Lichtensteiger, P. Hermet, S. Gariglio, J.-M. Triscone, and P. Ghosez, Nature (London) **452**, 732 (2008).

[4] H. N. Lee, H. M. Christen, M. F. Chisholm, C. M. Rouleau, and D. H. Lowndes, Nature (London) **433**, 395 (2005).

[5] M. Osada and T. Sasaki, Adv. Mater. **24**, 210 (2012).

[6] S. Zhong, S. Alpay, and J. Mantese, Appl. Phys. Lett. **88**, 132904 (2006).

[7] M. Ziese, I. Vrejoiu, E. Pippel, P. Esquinazi, D. Hesse, C. Etz, J. Henk, A. Ernst, I. Maznichenko, and W. Hergert, Phys. Rev. Lett. **104**, 167203 (2010).

[8] T. Zhao, Z.-H. Chen, F. Chen, W.-S. Shi, H.-B. Lu, and G.-Z. Yang, Phys. Rev. B **60**, 1697 (1999).

[9] A. Savoia, D. Paparo, P. Perna, Z. Ristic, M. Salluzzo, F. M. Granozio, U. S. di Uccio, C. Richter, S. Thiel, J. Mannhart, and L. Marrucci, Phys. Rev. B **80**, 075110 (2009).

[10] A. Ohtomo and H. Hwang, Nature (London) **427**, 423 (2004).

[11] R. J. Zeches, M. D. Rossell, J. X. Zhang, A. J. Hatt, Q. He, C. H. Yang, A. Kumar, C. H. Wang, A. Melville, C. Adamo, G. Sheng, Y. H. Chu, J. F. Ihlefeld, R. Erni, C. Ederer, V. Gopalan, L. Q. Chen, D. G. Schlom, N. A. Spaldin, L. W. Martin, and R. Ramesh, Science **326**, 977 (2009).

[12] V. Nagarajan, C. Jia, H. Kohlstedt, R. Waser, I. Misirlioglu, S. Alpay, and R. Ramesh, Appl. Phys. Lett. **86**, 192910 (2005).

[13] J. Zhang, D. Schlom, L. Chen, and C. Eom, Appl. Phys. Lett. **95**, 122904 (2009).

[14] O. Diéguez, K. M. Rabe, and D. Vanderbilt, Phys. Rev. B **72**, 144101 (2005).

[15] M. Dawber, N. Stucki, C. Lichtensteiger, S. Gariglio, P. Ghosez, and J. M. Triscone, Adv. Mater. **19**, 4153 (2007).

[16] M. Dawber, N. Stucki, C. Lichtensteiger, S. Gariglio, and J.-M. Triscone, J. Phys.: Condens. Matter **20**, 264015 (2008).

[17] J. Sinsheimer, S. Callori, B. Bein, Y. Benkara, J. Daley, J. Coraor, D. Su, P. Stephens, and M. Dawber, Phys. Rev. Lett. **109**, 167601 (2012).

[18] D. Kan, L. Pálová, V. Anbusathaiah, C. J. Cheng, S. Fujino, V. Nagarajan, K. M. Rabe, and I. Takeuchi, Adv. Funct. Mater. **20**, 1108 (2010).

[19] S. Fujino, M. Murakami, V. Anbusathaiah, S. H. Lim, V. Nagarajan, C. Fennie, M. Wuttig, L. Salamanca-Riba, and I. Takeuchi, Appl. Phys. Lett. **92**, 202904 (2008).

[20] E. V. Balashova and A. K. Tagantsev, Phys. Rev. B **48**, 9979 (1993).

[21] D. Kan, C. J. Cheng, V. Nagarajan, and I. Takeuchi, J. Appl. Phys. **110**, 014106 (2011).

[22] D. Kan, V. Anbusathaiah, and I. Takeuchi, Adv. Mater. **23**, 1765 (2011).

[23] A. Y. Borisevich, E. Eliseev, A. Morozovska, C.-J. Cheng, J.-Y. Lin, Y.-H. Chu, D. Kan, I. Takeuchi, V. Nagarajan, and S. V. Kalinin, Nat. Commun. **3**, 775 (2012).

[24] E. A. Eliseev, S. V. Kalinin, Y. Gu, M. D. Glinchuk, V. Khist, A. Borisevich, V. Gopalan, L.-Q. Chen, and A. N. Morozovska, Phys. Rev. B **88**, 224105 (2013).

[25] A. N. Morozovska, E. A. Eliseev, M. D. Glinchuk, L.-Q. Chen, and V. Gopalan, Phys Rev. B **85**, 094107 (2012).

[26] F. Le Marrec, R. Farhi, M. El Marssi, J. L. Dellis, M. G. Karkut, and D. Ariosa, Phys. Rev. B **61**, R6447(R) (2000).

[27] For samples beyond 17% Sm, the leakage contribution from the BSFO layers hindered the acquisition of reliable hysteresis loops.

[28] K. Kalantari, I. Sterianou, S. Karimi, M. C. Ferrarelli, S. Miao, D. C. Sinclair, and I. M Reaney, Adv. Funct. Mater. **21**, 3737 (2011).

[29] C. J. Cheng, D. Kan, V. Anbusathaiah, I. Takeuchi, and V. Nagarajan, Appl. Phys. Lett. **97**, 212905 (2010).

[30] See Supplemental Material at http://link.aps.org/supplemental/10.1103/PhysRevB.90.245131 for more details of experimental results. S1–S3 show detailed XRD and reciprocal space maps of the multilayers. S4 and S5 show in-depth profiles of polarization-electric-field loops, S6I and S6II provide detailed explanations of the thermodynamic theory used, and S7 presents loss tangent data for capacitance-voltage curves.

[31] S. Emery, C. J. Cheng, D. Kan, F. Rueckert, S. Alpay, V. Nagarajan, I. Takeuchi, and B. Wells, Appl. Phys. Lett. **97**, 152902 (2010).

[32] M. Dawber, C. Lichtensteiger, M. Cantoni, M. Veithen, P. Ghosez, K. Johnston, K. Rabe, and J.-M. Triscone, Phys. Rev. Lett. **95**, 177601 (2005).

[33] A. Morozovska, E. Eliseev, S. V. Kalinin, L. Q. Chen, and V. Gopalan, Appl. Phys. Lett. **100**, 142902 (2012).

[34] A. N. Morozovska, E. A. Eliseev, S. L. Bravina, A. Y. Borisevich, and S. V. Kalinin, J. Appl. Phys. **112**, 064111 (2012).

[35] E. A. Eliseev, M. D. Glinchuk, A. N. Morozovska, and Y. V. Yakovenko, Ukr. J. Phys. **57**, 1038 (2012).

[36] M. Glinchuk and A. Morozovska, J. Phys.: Condens. Matter **16**, 3517 (2004).

[37] M. D. Glinchuk, A. N. Morozovska, and E. A. Eliseev, J. Appl. Phys. **99**, 114102 (2006).

[38] A. N. Morozovska, E. A. Eliseev, and M. D. Glinchuk, Phys. Rev. B **73**, 214106 (2006).

[39] N. A. Pertsev, A. G. Zembilgotov, and A. Tagantsev, Phys. Rev. Lett. **80**, 1988 (1998).

[40] V. V. Lemanov, Fiz. Tverd. Tela **39**, 1468 (1997).

[41] V. A. Stephanovich, I. A. Luk'yanchuk, and M. G Karkut, Phys. Rev. Lett. **94**, 047601 (2005).

[42] J. X. Zhang, Y. L. Li, Y. Wang, Z. K. Liu, L. Q. Chen, Y. H. Chu, F. Zavaliche, and R. Ramesh, J. Appl. Phys. **101**, 114105 (2007).

[43] G. Catalan and J. F. Scott, Adv. Mater. **21**, 2463 (2009).

[44] P. Zubko, G. Catalan, A. Buckley, P. R. L. Welche, and J. F. Scott, Phys. Rev. Lett. **99**, 167601 (2007).

[45] S. H. Kogan, Sov. Phys.-Solid State **5**, 2069 (1964).